

Figures

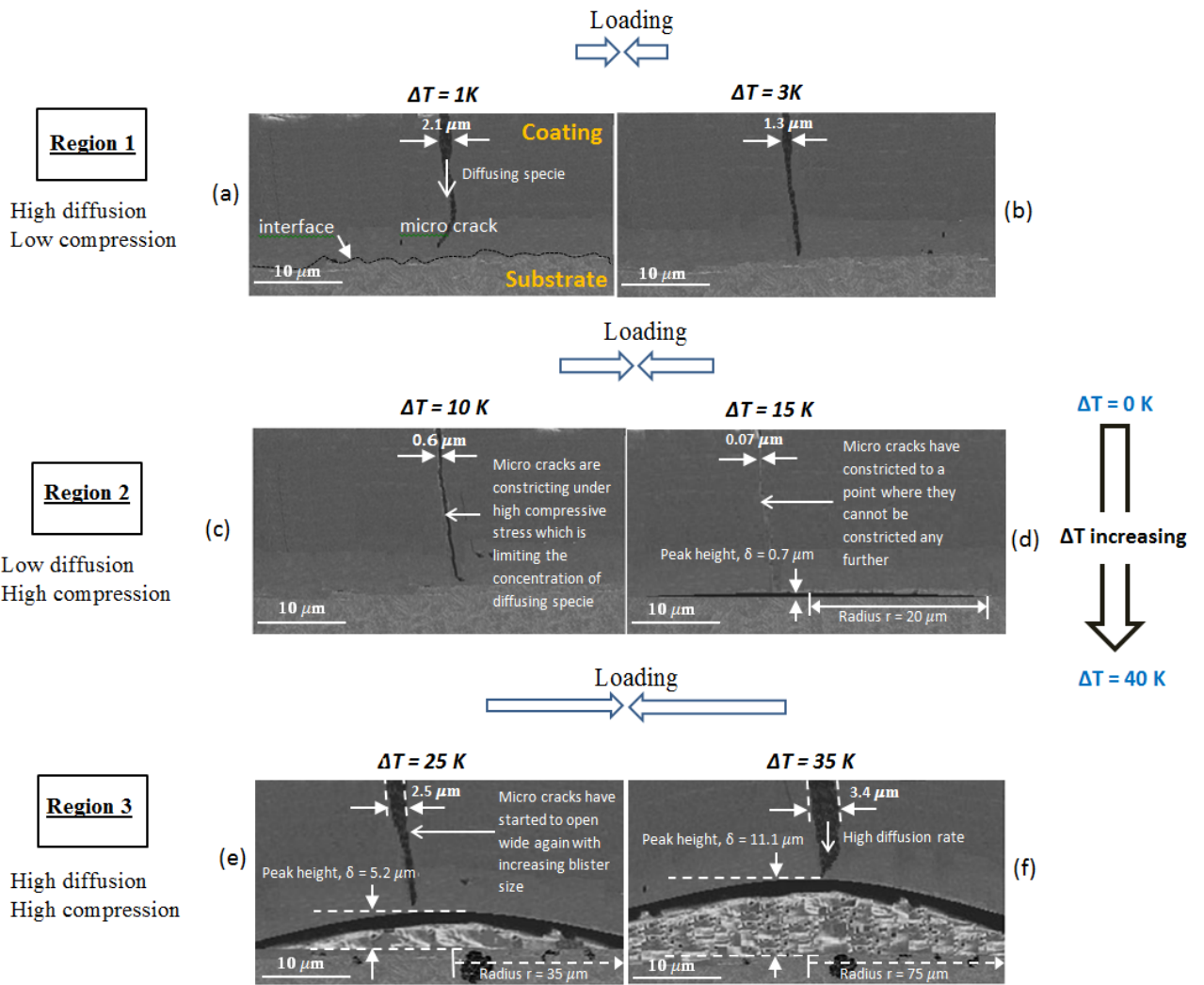


Figure 1. SEM images for three regions of blister initiation and propagation in the presence of coating micro-crack under the coupling effect of diffusion induced stress and compressive residual stress.

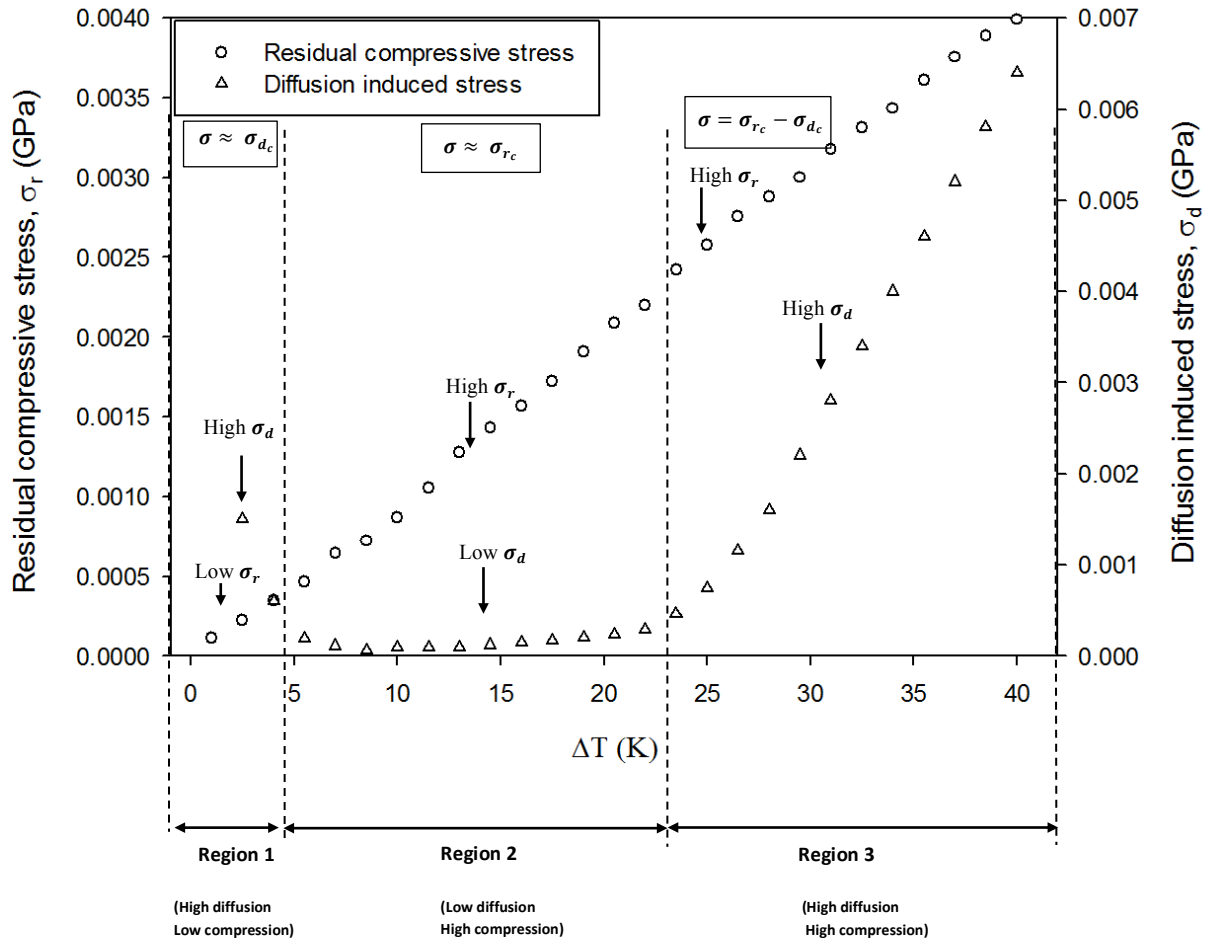
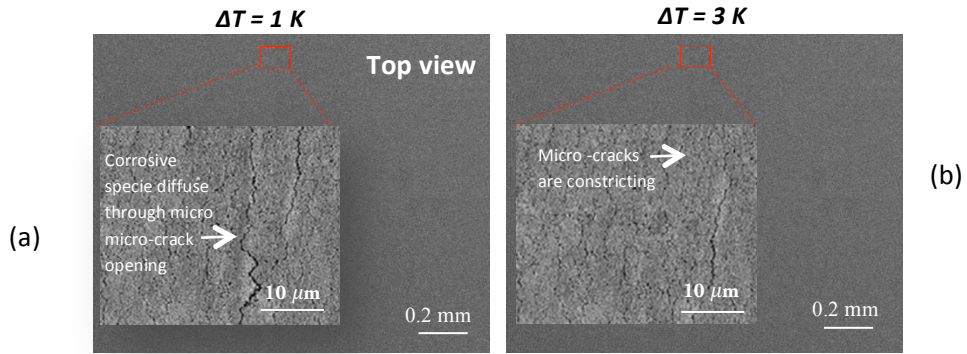
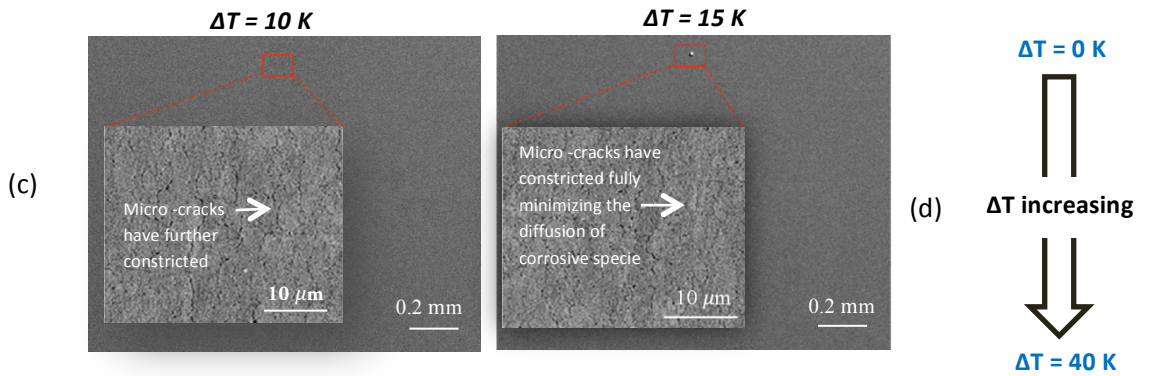


Figure 2. The stress graph for regions 1, 2 and 3 showing the values of diffusion induced stress and compressive residual stress with respect to increasing temperature ΔT .

Region 1: Pre-existing micro cracks at start of experiment



Region 2: High compressive stress causing the constriction of micro-cracks and blister nucleation



Region 3: Blister propagating

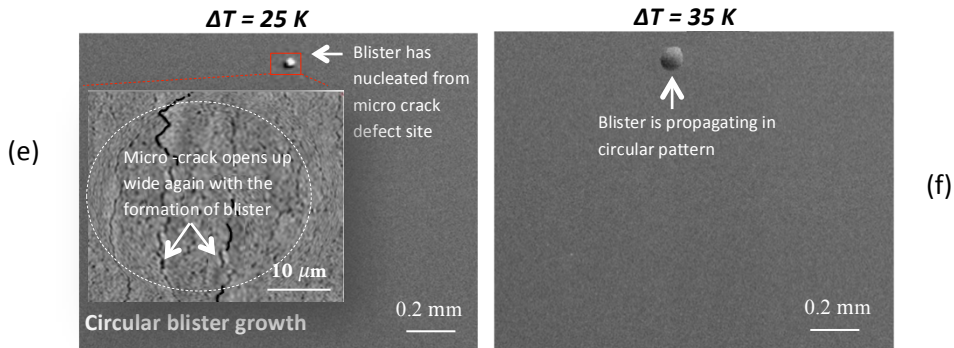


Figure 3. SEM images showing the top view of blistering initiation and propagation due to coupling effect of diffusion induced stress and residual compressive stress with respect to increasing temperature ΔT .

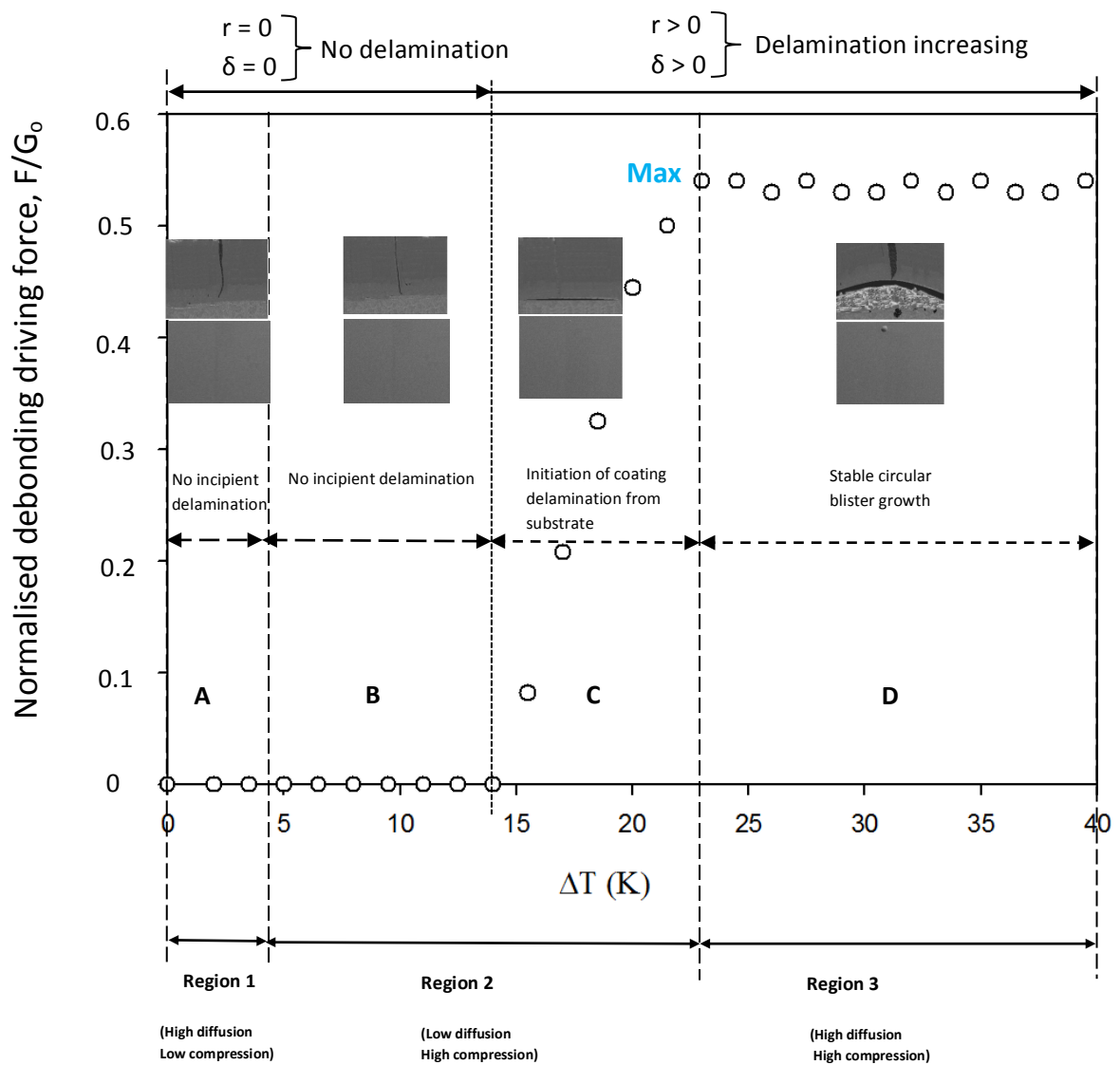
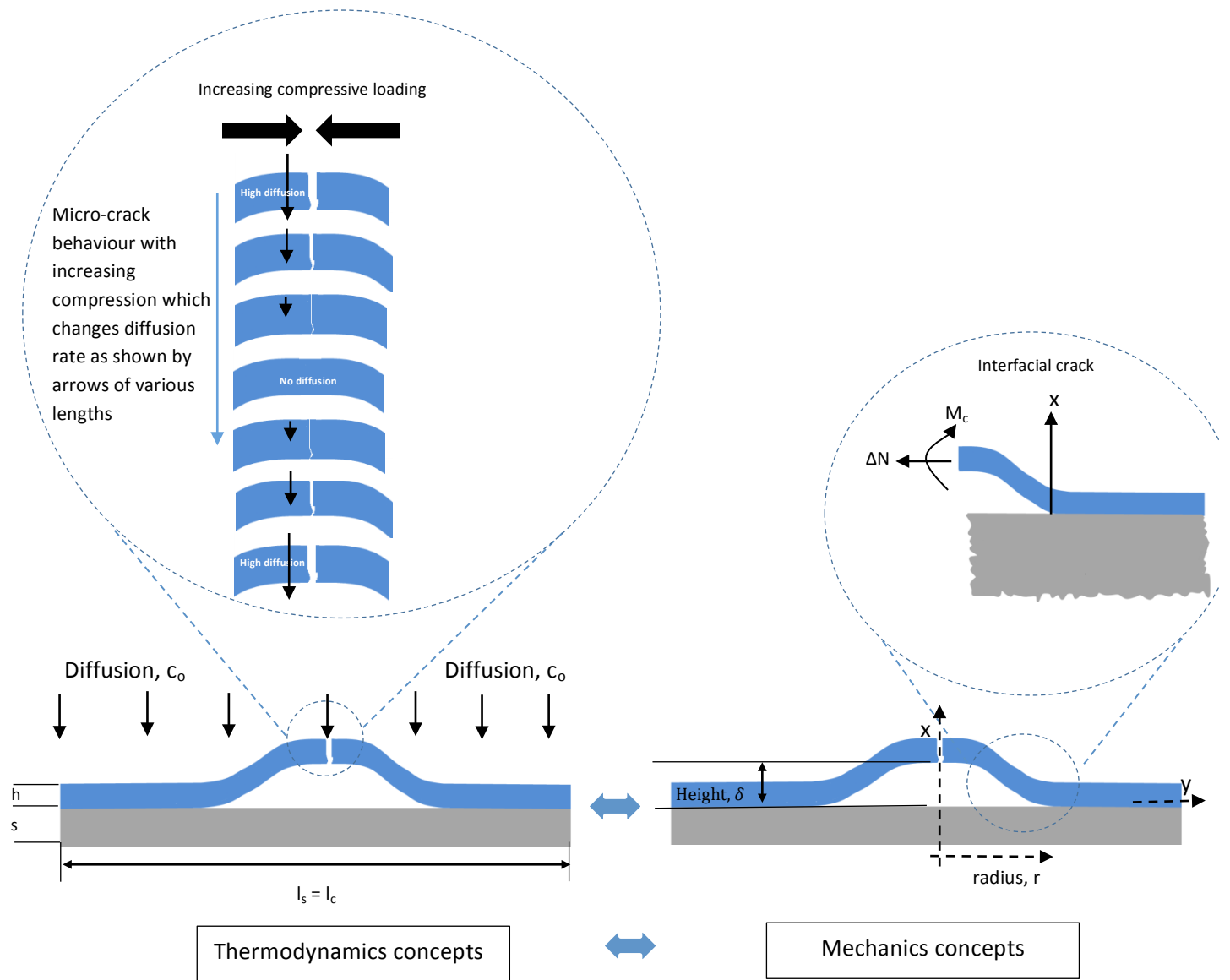
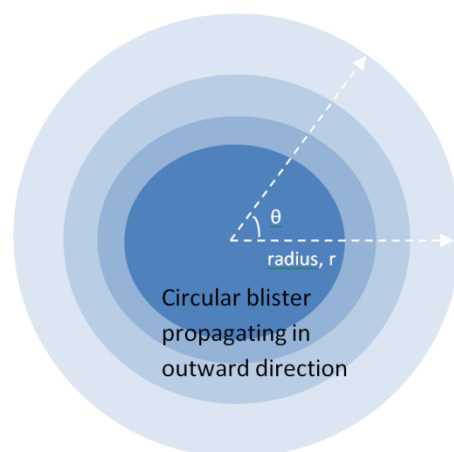


Figure 4. Debonding driving force as a function of increasing temperature ΔT . The behaviour of trend for debonding driving force as a function of increasing temperature ΔT can be divided in to four different zones: A, B, C and D. The debonding driving force is zero for zones A and B because in these two zones the coating is intact with the substrate. However, in zone C, the debonding driving starts to increase with the initiation of coating blistering. In zone D, the debonding driving force diminishes after reaching maxima Max with increasing ΔT .



(a)



(b)

Figure 5. Schematic showing (a) a “Two-part” theoretical model for blistering with micro-crack defect in coating. The left part of figure shows the diffusion concepts while the right part shows the mechanics concepts utilised in modelling. The length of arrow heads in diffusion part of figure shows the diffusion rate of species. (b) circular blister propagating in outward direction, which results in the increase in radius r of blister.

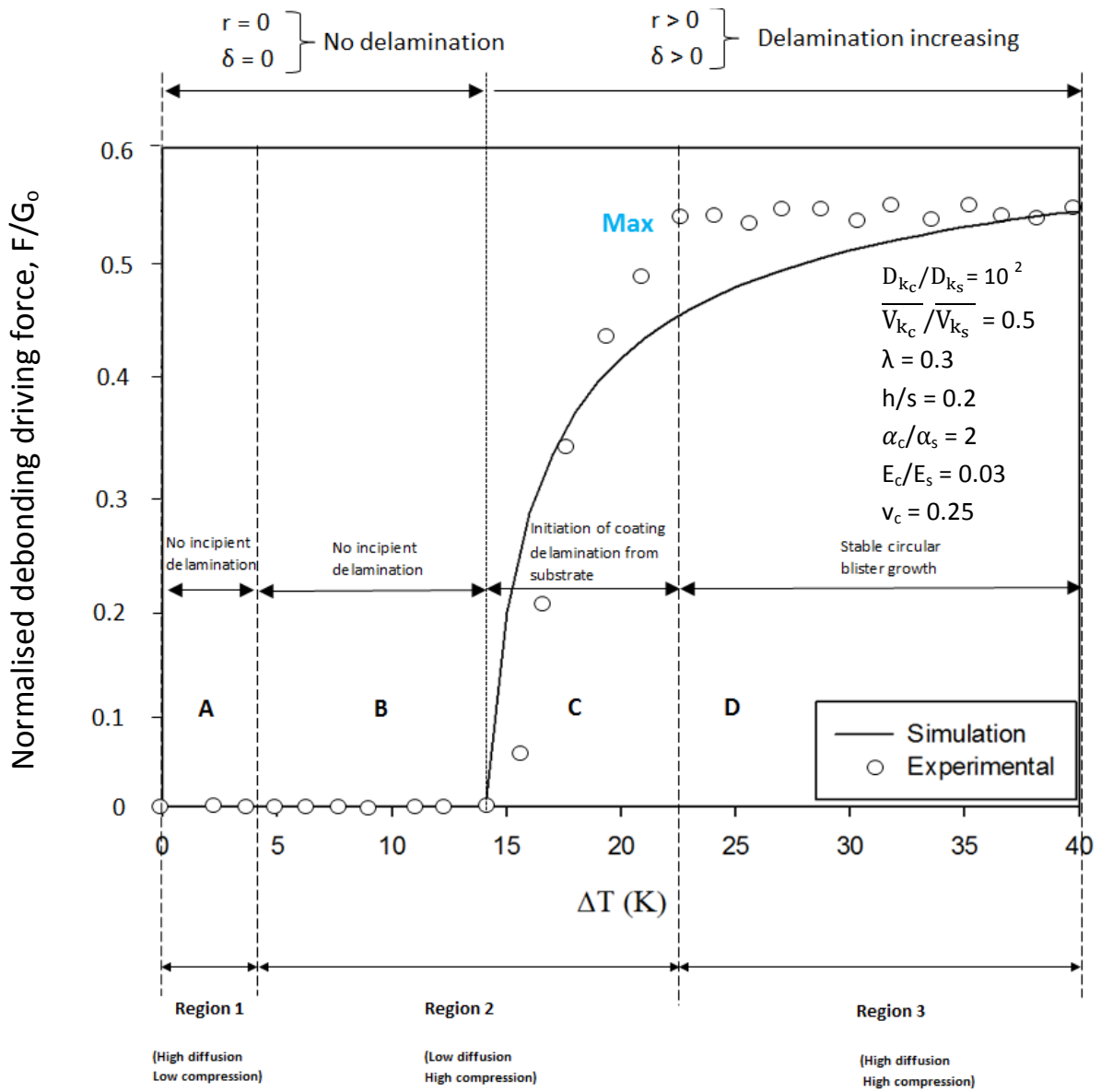


Figure 6. Simulation results for the effect of increasing temperature ΔT on the normalised debonding driving force. Figure also shows that the experiment and simulation trends both have a good qualitative agreement.

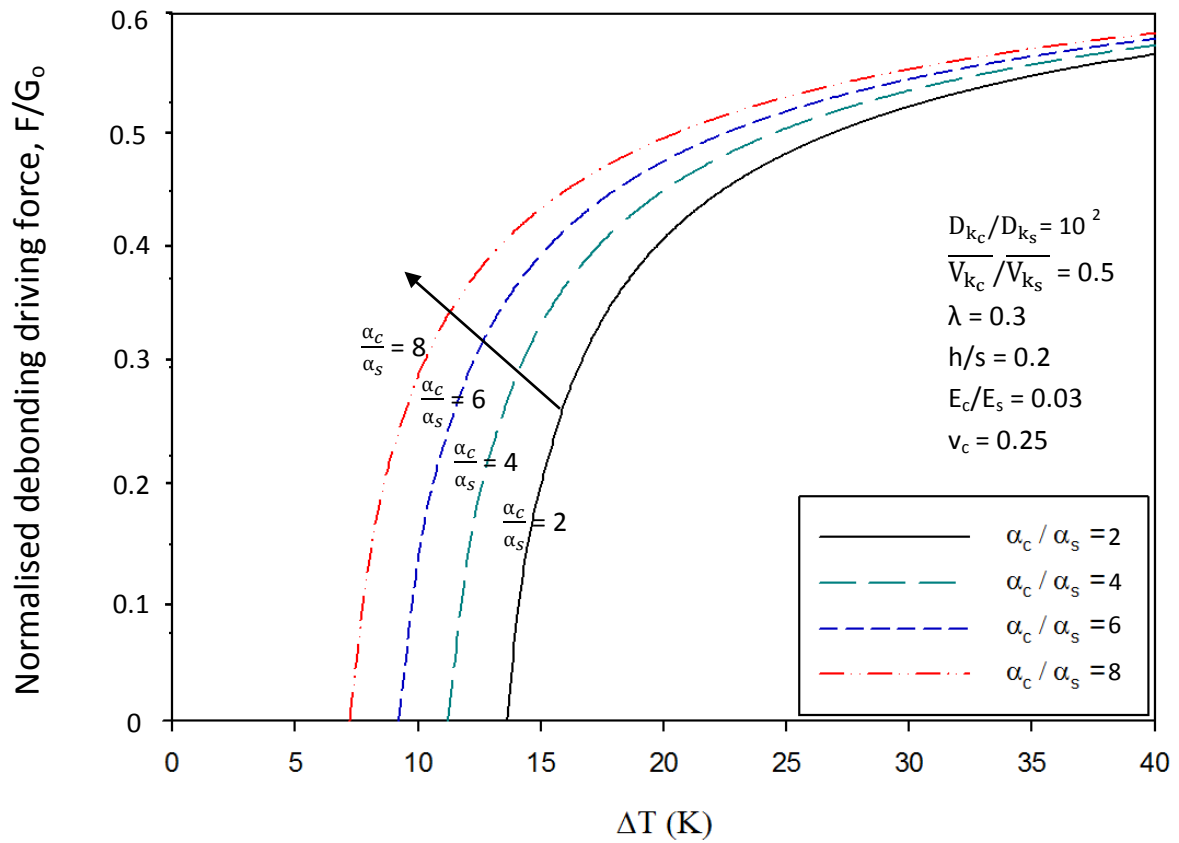


Figure 7. Effects of various values of coefficient of thermal expansion (CTE) mismatch α_c/α_s on normalised debonding driving force. It can be seen that as the CTE mismatch increases from $\alpha_c/\alpha_s = 2$ to $\alpha_c/\alpha_s = 8$, the normalised debonding driving force as a function of temperature ΔT also increases.

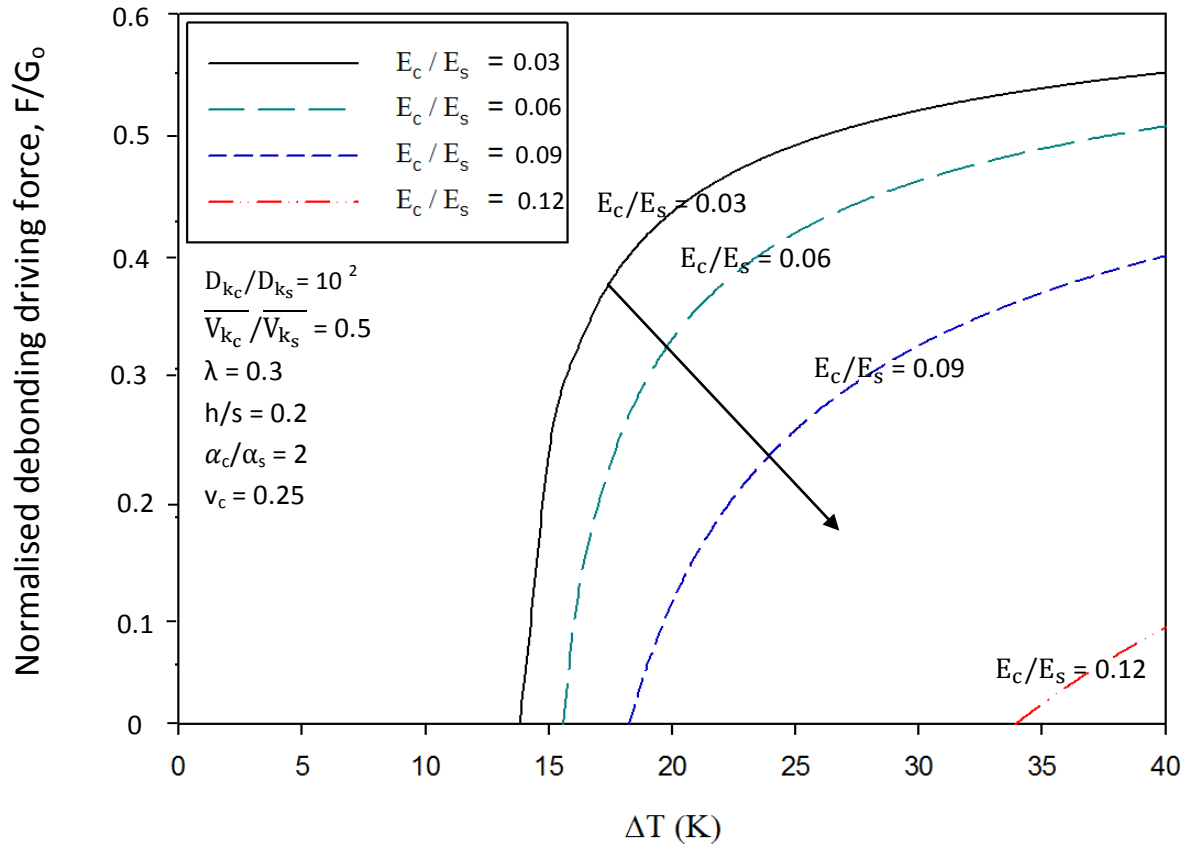


Figure 8. The evolution of normalised debonding driving force corresponding to various values of moduli ratio E_c/E_s . It can be seen that the normalised debonding driving force increases with the decrease in moduli ratio E_c/E_s .

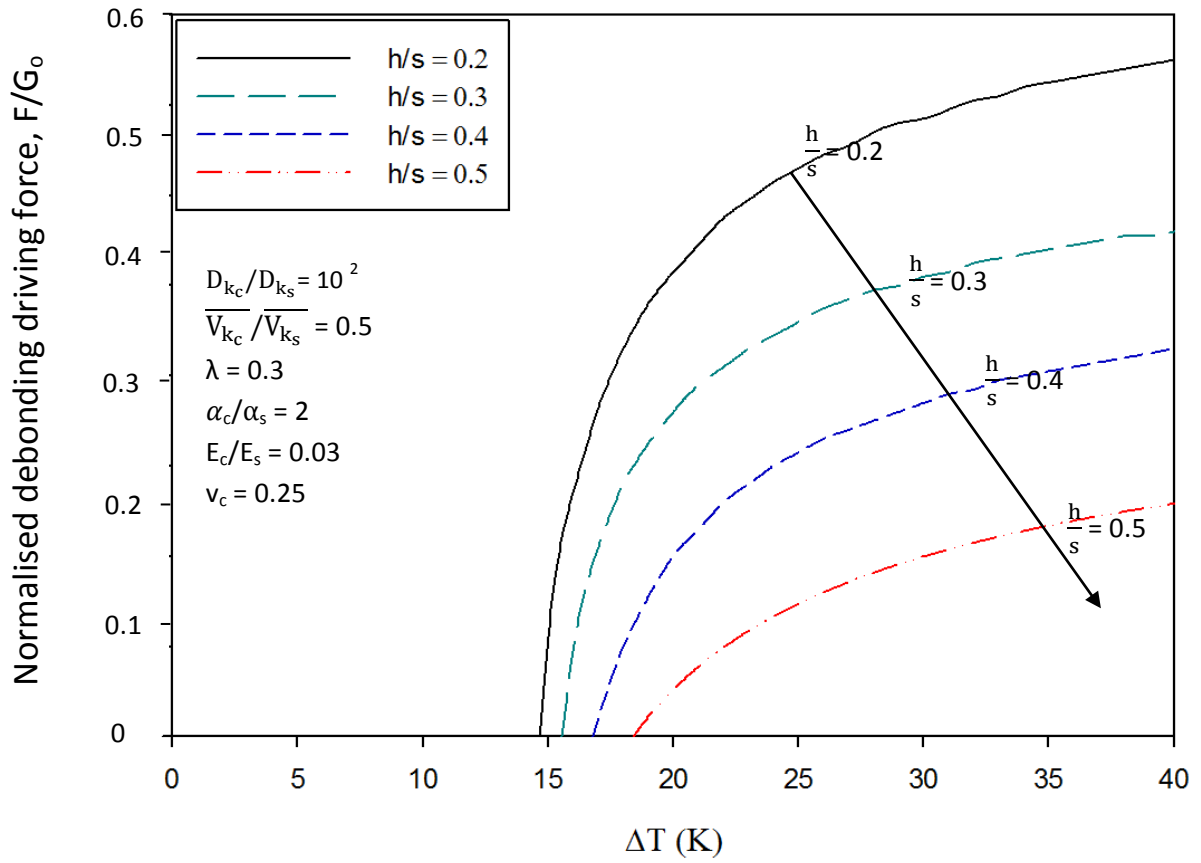


Figure 9. The effects of thickness ratio h/s on normalised debonding driving force. It can be seen that the normalised debonding driving force F/G_0 increases with increasing temperature ΔT for various values of h/s

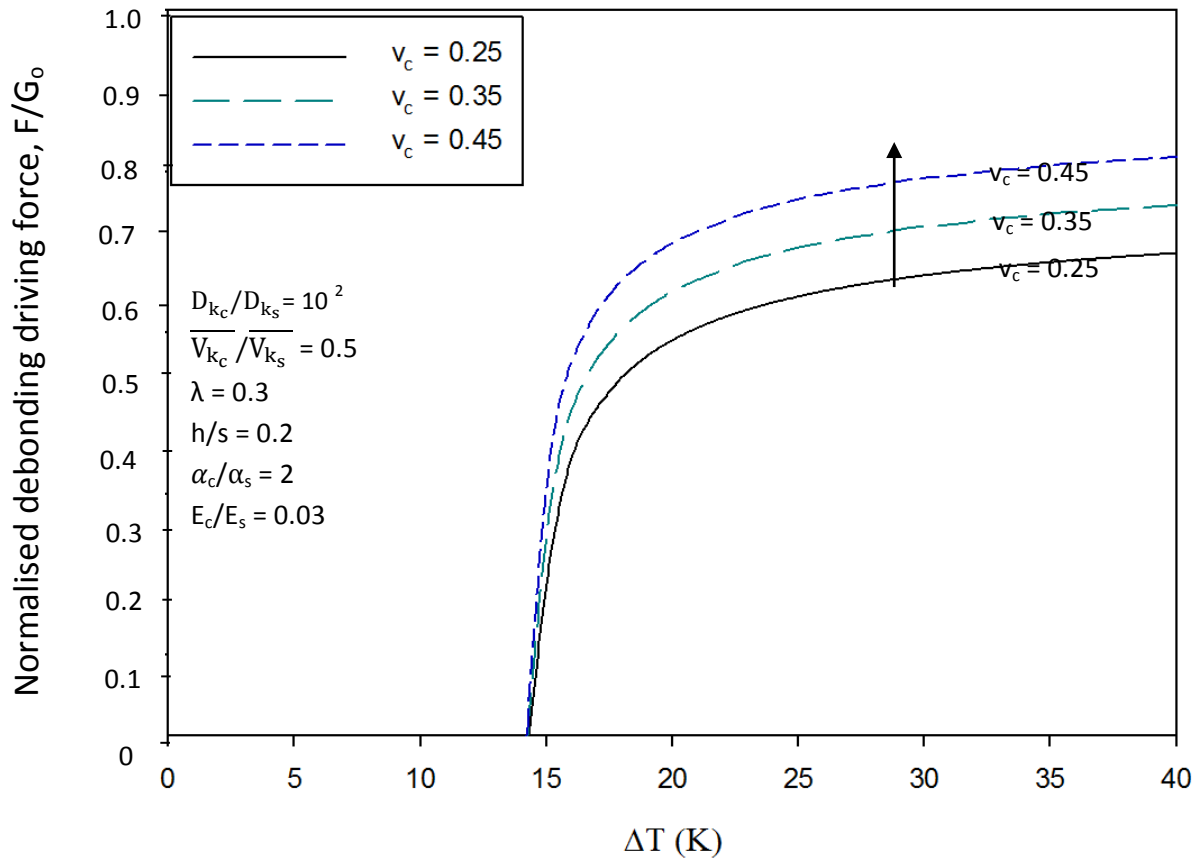


Figure 10. The trends of normalised debonding driving force with increasing temperature ΔT for various values of coatings poisson's ratio ν_c . It can be seen that the normalised debonding driving force increases with the increase in value of ν_c

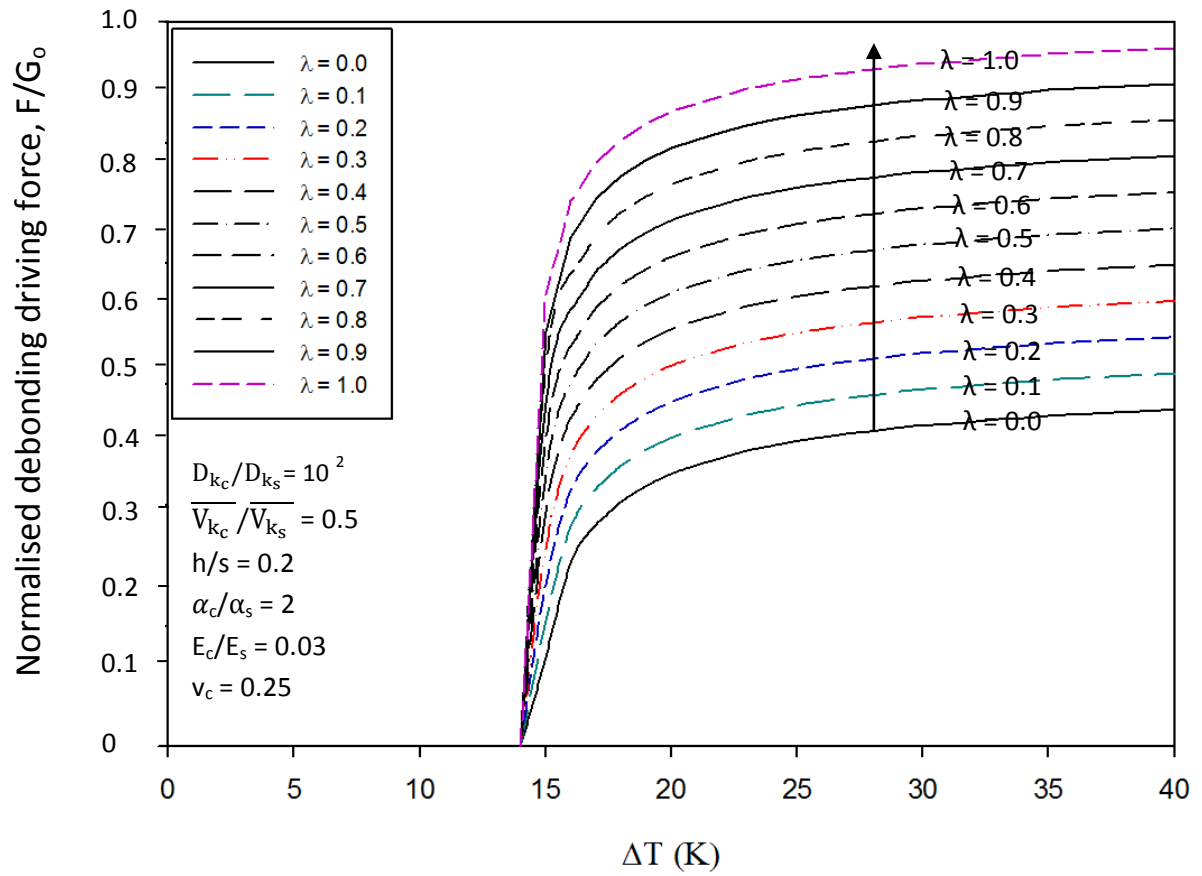


Figure 11. The effect of various values of roughness parameter λ on normalised debonding driving force with increasing temperature ΔT . It can be seen that the normalised debonding driving force F/G_0 increases with the increase in λ .